Journal of Materials Chemistry A

ROYAL SOCIETY OF CHEMISTRY

PAPER

View Article Online
View Journal | View Issue

Cite this: J. Mater. Chem. A, 2025, 13, 12383

Electrocatalytic hydrogenation of unsaturated organics using Mo and W porous carbon-encapsulated nanostructures: impact of metal type on properties and performances†

Filippo Pota, [a] Maida Aysla Costa de Oliveira, [a] Christian Schröder,[a] Aran Rafferty, [a] Clara De Castro,[b] Ludivine Rault,[c] James A. Behan,[d] Frédéric Barrière[d] and Paula E. Colavita *[a]

Electrocatalytic hydrogenation (ECH) of organics of biomass origin represents a promising strategy to enable integration of renewables and circular economy practices. However, most electrocatalysts investigated for ECH remain largely based on precious metals. Nanostructured materials based on transition metals encapsulated in a nitrogenated carbon matrix (M@C:N) offer a promising alternative. Herein, we report on the synthesis of Mo@C:N and W@C:N composites that display the same metal atomic concentrations and thus allow for a comparative study of the effect of the metal centre identity on the properties of such heterostructured materials and their performance in the ECH of benzaldehyde, a diagnostic organic substrate. A combination of structural characterisation methods indicates that the type of metal impacts carbon porosity and metal surface concentration in the synthesised structures. W displays a higher tendency to yield encapsulated nanoparticles compared to Mo, which is instead present with surface excess but at predominantly high oxidation states. Electrolysis studies at varying potentials demonstrate high product rates of benzaldehyde hydrogenation, with good selectivity for the production of the corresponding alcohol *vs.* the dimerization side product. Turnover frequency (TOF) estimates under the operational conditions tested suggest that replacing Mo-centres with W-centres in M@C:N architectures improves overall performance. A comparison of performance indicators with those for Pt-group metals suggests that W@C:N could be a competitive material for practical implementations of ECH.

Received 17th December 2024
Accepted 21st March 2025

DOI: 10.1039/d4ta08953g

rsc.li/materials-a

1. Introduction

The development of efficient and high-performing catalysts for electrochemical processes is essential for the advancement of energy technologies and biomass-valorisation strategies.[1,2] Electrocatalytic hydrogenation (ECH) is a sustainable and versatile approach for the reduction of various organic compounds, including those of biomass origin, using renewables as an energy source.[2,3] ECH is appealing due to its potential for fine-tuning reaction conditions, reducing carbon emissions, and enabling reactions under mild conditions compared to conventional hydrogenation processes that often require high pressures and temperatures.[4] Moreover, ECH offers opportunities for carrying out selective hydrogenations, which are highly desirable for the production of pharmaceuticals, agrochemicals, and fine chemicals.

Electrocatalysts for ECH processes are generally still based on precious metals such as Pd, Pt, Au[5–7] and their alloys, or on carbon-supported precious metals (M/C) such as Pt/C, Pd/C, and Ru/C.[8–11] Since the above elements can command market prices ranging from 15 to 90 USD per g,[12] there is an ongoing research effort to develop abundant and low-cost electrocatalysts as viable alternatives. Recently, the use of metal nanostructures encapsulated within N-doped carbon architectures (M@C:N) has emerged as a promising strategy for the preparation of materials with ECH activity.[13] M@C:N materials have received significant attention as electrocatalysts for a range of cathodic processes of high importance in energy technologies, including the hydrogen evolution reaction (HER), and the reduction of O_2 and CO_2.[14–20] M@C:N heterostructures can display unique properties such as high surface area and tuneable surface electronic structure and chemical reactivity.[18] Moreover, the presence of a carbon shell that protects the metal

[a]School of Chemistry, Trinity College Dublin, College Green, Dublin 2, Ireland. E-mail: colavitp@tcd.ie

[b]Earth Surface Research Laboratory, Geology Department, Trinity College Dublin, College Green, Dublin 2, Ireland

[c]Univ Rennes, CNRS, ScanMAT – UAR 2025, Rennes, F-35000, France

[d]Univ Rennes, CNRS, Institut des Sciences Chimiques de Rennes – UMR 6226, Rennes, F-35000, France

† Electronic supplementary information (ESI) available. See DOI: https://doi.org/10.1039/d4ta08953g

from oxidation due to air exposure or from corrosion in aqueous solutions can expand the range of metals used for electrocatalysis to encompass low-cost and earth abundant transition metals, enhancing the versatility and stability advantages of M@C:N architectures.[18,21] However, development of M@C:N architectures for ECH still presents significant challenges and little is known about how to optimize both the metal core and the graphitised scaffold to improve ECH performances. Organic hydrogenations must progress with efficiency under electrochemical conditions at which the HER is typically a competing reaction. The Volmer reaction step leading to H_{ads} activation at the electrocatalyst surface is a requirement for both the HER and the ECH to take place.[22] However, these two reactions compete for this intermediate to yield final products: indeed the Tafel and Heyrovsky steps in the HER consume H_{ads} species and may drastically suppress the faradaic efficiency (FE) of organic hydrogenations.[11]

Previous work from our group demonstrated for the first time that M@C:N electrocatalyst materials synthesised using a low cost transition metal such as iron are active in the ECH of carbonyl compounds. In this work, we show that this material design strategy can be expanded to incorporate alternative transition metals into the electrocatalyst, namely W and Mo, enabling the optimisation of ECH performance indicators in M@C:N architectures. Mo and W are highly desirable as metal cores due to their significantly lower costs compared to precious metals, with market prices of *ca.* 0.07 USD per g and 0.05 USD per g, respectively.[12] Further, these metals and several of their compounds also possess the ability to activate chemisorbed hydrogen through the Volmer step while displaying differences in their activity towards hydrogen evolution,[18,23,24] thus offering a potential route to regulating the degree of competition between the HER and the ECH. Benzaldehyde (BZH) was used as a model organic compound due to its solubility in water[25,26] and because it enables quantitative benchmarking of performance indicators relative to other results in the ECH literature.[27–29] Our results demonstrate that the identity of the metal core can have a profound influence on the properties of the graphitised carbon matrix and on the surface chemical composition in M@C:N materials with identical atomic metal loadings. This translates into important changes in product rates, faradaic efficiencies and turnover frequencies thus providing new insights on how to optimise transition metal-based heterostructured electrocatalysts for the ECH of organics.

2. Material and methods

2.1 Materials

Nafion® 117 solution (5%), resorcinol (99%), Pluronic F-127, melamine (99%), hydrochloric acid (37%), sulfuric acid (95–98%), nitric acid (≥65%), formaldehyde solution (37 wt%), hydrogen peroxide (30%), sodium sulfate (>99%); benzaldehyde (BZH, >99%); hydrobenzoin (HBZ, 99%); acetophenone (>99%); ethyl acetate (>99%); ammonium heptamolybdate tetrahydrate ($(NH_4)_6Mo_7O_{24}\cdot 4H_2O$, 99%) were all purchased from Sigma Aldrich and used as received. Methanol (>99%), benzyl alcohol (BA, >99%) and ammonium metatungstate hydrate ($(NH_4)_6W_{12}O_{39}\cdot H_2O$, 99%) were purchased from Fisher and used as received. Black Pearls 2000® (BP, >1400 $m^2\ g^{-1}$)[30,31] were purchased from Cabot.

2.2 Methods

BP were purified under reflux in concentrated HNO_3 at 90 °C for 4 h, then filtered and washed until reaching a neutral pH.[13] Porous carbon-based catalysts were synthesised by first dissolving resorcinol (0.83 g), Pluronic F-127 (1.25 g), and melamine (0.42 g) in 20 mL of a 1 : 1 water : methanol solution and stirring for 15 min. Ammonium heptamolybdate tetrahydrate $(NH_4)_6Mo_7O_{24}\cdot 4H_2O$, or ammonium metatungstate hydrate $(NH_4)_6W_{12}O_{39}\cdot H_2O$, were then added as metal precursors in amounts summarised in Table 1, followed by the addition of concentrated HCl (0.2 g) and stirring for 1 h. Formaldehyde (1.25 g) was introduced dropwise, resulting in a homogeneous slurry after vigorous stirring for another hour. Purified BP (0.75 g) was added to the mixture and stirred for an additional 15 min. The mixture was heated in a Teflon-lined autoclave at 50 °C for 2 days, then the vessel was opened and the solid was thoroughly dried at the same temperature. The sample was ground in a mortar, inserted in a tube furnace at 250 °C under N_2 flow and, finally, annealed at 800 °C for 2 h in a N_2 : NH_3 flow (1 : 1 vol., 200 sccm total) following the procedure reported previously.[13]

2.3 Materials characterisation

Brunauer–Emmett–Teller (BET)[32] specific surface area was determined from N_2 adsorption at 77 K with a Nova 2200e surface area analyzer (Quantachrome, UK). The specific surface area was calculated from data in an optimal relative pressure range according to the method proposed by Rouquerol *et al.*,[33] by way of the micropore BET assistant feature of the NovaWin software. Pore size distributions were determined using the density functional theory (DFT) method[34,35] based on the calculation model: N_2 at 77 K on carbon (slit pore, NLDFT equilibrium model). Prior to analysis, the samples were outgassed at 250 °C under vacuum for 2 h. Thermogravimetric analysis (TGA) was carried out using a Pyris 1 thermogravimetric analyser (PerkinElmer) with a hold time of 10 min at 150 °C, followed by a 10 °C min^{-1} ramp in air to 900 °C. Powder X-ray diffraction (XRD) was carried out using a D2 Phaser diffractometer with LynxEye detector (Bruker) and a Cu Kα source. Scanning electron microscopy (SEM) was performed using a Zeiss Ultra microscope at 5 kV accelerating voltage with an SE2 detector. High resolution transmission electron microscopy (HR-TEM) was performed using a Jeol JEM 2100HR at 200 kV using EDS SDD Oxford X-Max 80T detector. Inductively coupled plasma-optical emission spectroscopy was performed in a iCAP 7000 ICP-OES analyser (Thermo Fisher); samples were treated in HNO_3 (≥65%) overnight and diluted in deionised water to a nominal concentration of 10 mg L^{-1}. Energy-dispersive X-ray fluorescence analysis (XRF) was performed using a Rigaku ED-XRF in He atmosphere on bulk solid samples. X-ray photoelectron spectroscopy (XPS) was carried out in a monochromated Omicron XM1000MK II X-ray

Table 1 Summary of samples, details of the metal precursors used, metal content after the final graphitisation step by weight-% and by atomic-%, and BET specific surface area

Material	Metal precursor	Initial metal precursor (g)	wt. (%)	at. (%)	BET ($m^2\ g^{-1}$)
Mo@C:N	$(NH_4)_6Mo_7O_{24}\cdot 4H_2O$	1.78	10.8[a]	1.51	229
W@C:N	$(NH_4)_6W_{12}O_{39}\cdot H_2O$	0.61	17.7[b]	1.41	450
RPM/BP	N/A	N/A	N/A	N/A	600

[a] Data obtained by ICP-OES on the graphitised material. [b] Data obtained by ED-XRF on the graphitised material.

photoemission spectrometer, with an EA 125 analyser and an Al Kα (1486.7 eV) source; pass energies of 50 and 15 eV were used for survey and high-resolution spectra, respectively. Spectra were analysed using CasaXPS; best fits were carried out on spectra after Shirley background correction using mixed Gaussian–Lorentzian functions. Elemental compositions were obtained from peak areas of the high-resolution scans after correction for relative sensitivity factors. Product analysis was carried out using an Agilent 8860 gas chromatograph coupled to a flame ionisation detector (GC-FID), H_2 as carrier gas, split injection (1 : 10, 2 mL min^{-1} flow) and a DB-WAX UI column (30 m × 0.250 mm × 0.50 μm, Agilent J&W).

2.4 Electrochemical characterisation

Synthesised materials were mortared and sieved (20 μm) prior to the preparation of catalyst inks. Ink dispersions contained catalyst (0.0100 g ± 0.0003), 270 μL of deionised water, 160 μL of methanol (MeOH) and 53 μL of Nafion solution. Each addition was followed by 10 min of sonication in a cooling bath; the resulting dispersion was drop-cast on carbon working electrodes for further analysis. Glassy carbon disks (GC, Ø 5 mm, HTW GmbH) were used as working electrodes for cyclic voltammetry experiments. GC disks were polished with decreasing grades of alumina slurry (Ted Pella) according to published procedures;[36] disks were thoroughly sonicated and rinsed between polishing steps to remove any residue from the preceding step. GC disks were mounted in a Teflon disc holder (Pine instruments) and modified with the ink dispersion (10 μL), then dried under inert gas, resulting in a loading of 1.06 mg cm^{-2}. Flags of carbon cloth (CC, 1 cm^2 geometric area, FuelCellStore) with microporous layer were used as current collectors for electrolysis experiments. The CC was used as received after covering the back side with insulating polyimide tape. 52 μL of the ink were drop-cast in two equal aliquots, drying the ink after each step in a hot plate (80 °C), followed by compression of the CC in a hydraulic press (Specac) at room temperature; this resulted in loadings of 1.07 mg cm^{-2} for all samples. Voltammetry experiments were carried out using a standard 3-electrode cell controlled by a potentiostat (Metrohm Autolab), using graphite rods (Morgan advanced materials) as counter electrodes and Ag/AgCl (1 M KCl) as reference electrode (0.235 V *vs.* SHE). All potentials are reported *vs.* the relative hydrogen electrode (RHE) based on the experimentally determined pH of the electrolyte. The cell was cleaned with piranha and deionised water prior to each experiment, then filled with 250 mL volume of supporting electrolyte (0.100 M H_2SO_4); the electrolyte was purged with N_2 for at least 15 min prior to characterisation. Electrolysis was performed in a customised H-cell thermostated at 25 °C as previously reported.[13] Quantitative analysis was conducted *via* GC-FID after extraction with ethyl acetate, using acetophenone as internal standard.

3. Results and discussion

Carbon-based materials were synthesised using a procedure described in our previous study[13] and schematically illustrated in Fig. 1a. Briefly, materials were synthesised *via* polycondensation of resorcinol and formaldehyde with the addition of BP carbon black as a conductive scaffold, Pluronic F-127 as a soft template and melamine as a nitrogen source. Annealing at 800 °C under N_2/NH_4 atmosphere resulted in graphitisation, yielding a material from here onwards referred to as RPM/BP. Metal precursors can also be added to this procedure to achieve metal encapsulation in a M@C:N architecture.[13,37] In this work, we integrated Mo and W metal precursors into the established protocol; Table 1 shows the precursor quantities used for the synthesis of each sample, as well as the metal content obtained after the final graphitisation step in the synthesis, by weight and by atomic percent. The bulk composition of Mo-based materials was investigated *via* ICP-OES, while for W-based electrodes ED-XRF analysis was performed. The atomic-% content in the bulk was calculated assuming carbon and metal to be the main components. The two M@C:N materials exhibit similar metal atomic content of *ca.* 1.5% and can therefore be used to compare the effects of a change of metal on the nanocomposite structure and its electrochemical performance.

The bulk structure of the materials was first investigated *via* XRD; Fig. 1b reports patterns collected for metal-free RPM/BP, Mo@C:N and W@C:N. RPM/BP materials yielded two peaks at 24.3° and 43.2°, indexed as (002) and (101) reflections of the graphitic carbon,[38] respectively. The Mo@C:N pattern indicates the presence of crystalline phases consisting of mostly Mo_2C, with contributions from MoO_2 oxide. Peaks at 34.4°, 37.8°, 39.3°, 51.9°, 61.5°, 69.3°, 74.4°, 75.6°, match well those Mo_2C reference (PDF#35-0787) and are assigned to reflections (100), (002), (101), (102), (110), (103), (112) and (201), respectively. The broad peak at 25.3° is assigned to (002) reflection of graphitic carbon and matches the main reflection in the pattern of metal-free RPM/BP. The small broad peak at 36.9° indicates the presence of MoO_2 (PDF#65-5787) as well. The XRD pattern for

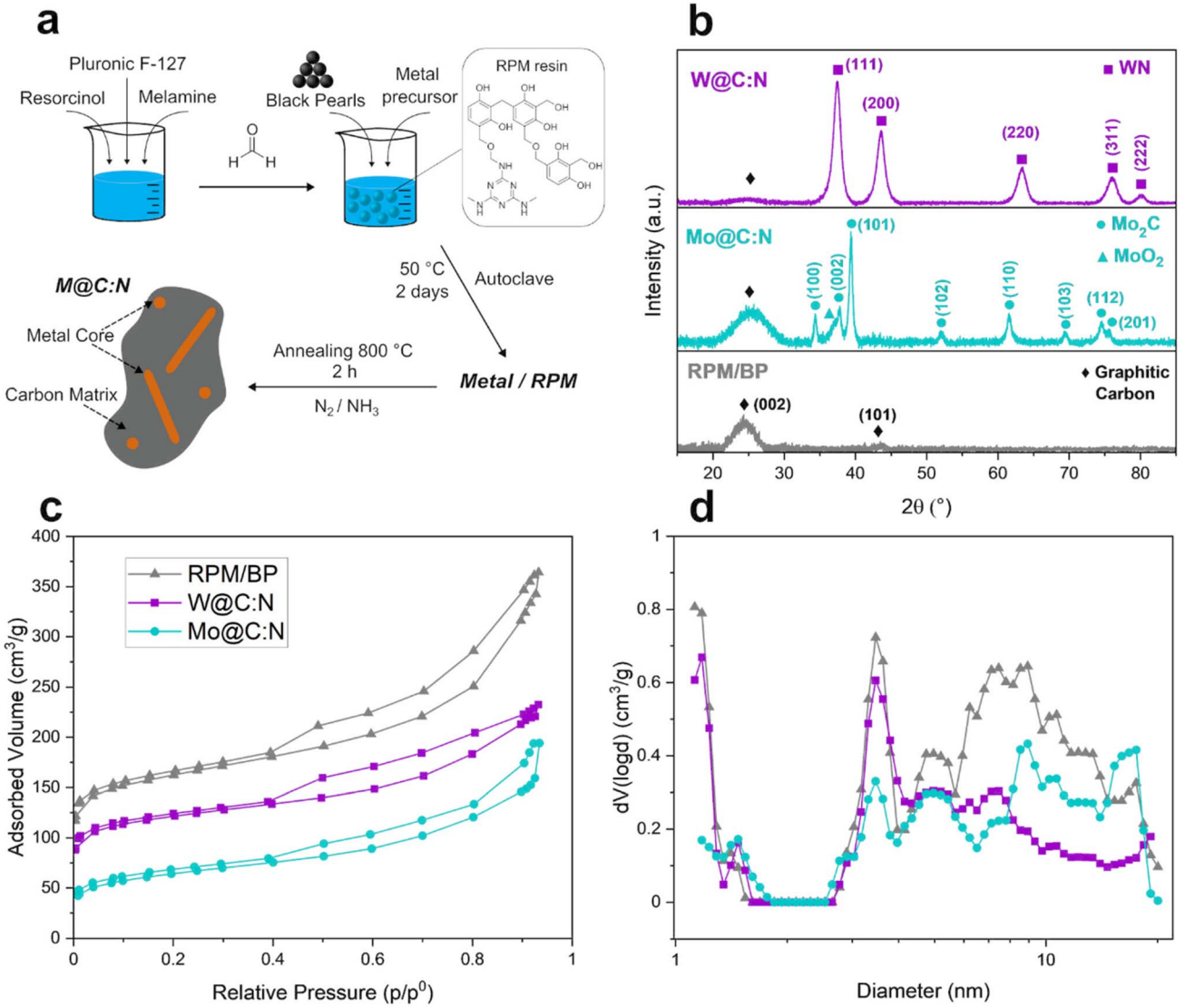

Fig. 1 (a) Scheme illustrating main steps of the materials synthesis protocol. (b) XRD patterns for metal-free RPM/BP, Mo@C:N and W@C:N. (c) Nitrogen adsorption–desorption isotherms and (d) pore size distributions for RPM/BP, W@C:N and Mo@C:N materials.

W@C:N shows peaks at 37.4°, 43.6°, 63.3°, 76.1° and 80.1°, that match those of the WN reference pattern (PDF#65-2898) and are assigned to reflections (111), (200), (220), (311), and (222), respectively.[39,40] The (002) reflection of graphitic carbon is also detectable at 24.6°.

Synthesised materials were found to be porous; Fig. 1c shows the N_2 adsorption/desorption isotherms collected for Mo@C:N, W@C:N and the metal-free RPM/BP. Samples display similar hysteresis loops characteristic of type IV isotherms, associated with capillary condensation, and type H4 loops reported for narrow slit-like micro-/mesopores.[41,42] The BET specific surface area values calculated from the isotherms are summarised in Table 1. The incorporation of Mo or W into the structure results in a decrease in BET surface areas by 15% to 67% compared to metal-free RPM/BP. Assuming that contributions to the surface area from metal-containing phases are negligible relative to those from the carbon phases, and accounting for the metal wt% in Table 1, it is possible to note that for W@C:N the BET area is only slightly lower than expected from a replacement of 1.4% of C atoms in RPM/BP with W (494 $m^2 g^{-1}$). This suggests that the development of the carbon microscopic area during graphitisation is not significantly affected by the presence of the W centres at these concentrations. On the other hand, for Mo@C:N the BET area is less than half the value expected based on replacement of 1.5% of C atoms alone (535 $m^2 g^{-1}$). This suggests that Mo centres impact the development of pores in the carbon phase to a much greater extent than W. Metal centres can have a catalytic effect on carbon gasification and graphitisation,[37,43–47] and such processes can enhance pore opening and lead to reductions in BET areas.

To better understand the impact on pore size, the DFT method was used to generate pore size distributions (PSD), shown in Fig. 1d. The three materials are similar insofar as they exhibit distinct occurrences of porosity in the micro (<2 nm)

and meso (2–50 nm) ranges, with broadly similar distributions, *i.e.* peaks at 1.5, 3.5 and 5 nm, characteristic of the parent carbon phase. W@C:N and RPM/BP share the most obvious similarities, with a significant volume of micro-pores, which are key contributors to the surface area. A closer inspection of the micropore region shows differences, in that the second peak (*ca.* 1.5 nm) grows according to Mo@C:N > W@C:N > RPM/BP, while the peak at 1.1 nm decreases accordingly. In other words, larger micropores are generated at the expense of smaller ones. Notably, Mo@C:N displays limited contributions from micro-pores relative to both RPM/BP and W@C:N. This likely explains the lower surface area observed for this sample, as well as its low pore volume (Table S1†). Further, it highlights a key difference between Mo@C:N and W@C:N: for Mo@C:N the smallest tranche of micropores have either been rendered inaccessible or have undergone enlargement. DFT pore width values (mode), in Table S1,† show that pore size increases with a decrease in surface area, as expected. Of note is the fact that the values for RPM/BP and W@C:N occur in the micropore range, where that of Mo@C:N falls in the mesopore range thus confirming that pore evolution in the N-doped carbon matrix is significantly affected by the incorporation of Mo centres.

TGA analysis in air was carried out and results are reported in Fig. S1.† Briefly, in the case of the metal-free RPM/BP a single combustion process with zero residual mass is observed over 650–750 °C, associated with oxidation of graphitised carbon. In the presence of metals, carbon oxidation occurs at significantly lower temperatures, with the effect on onset temperature being more pronounced in the case of Mo-containing materials. This is consistent with oxidation being catalysed by metal centres, in agreement with prior literature;[48,49] while the enhanced effect of Mo *vs.* W in these reactions is also consistent with observations from BET and DFT analysis that suggest a greater effect of Mo centres on pore opening processes.

Morphology was investigated *via* electron microscopy. Fig. 2a shows an SEM image of Mo@C:N, revealing particles with rough and irregular surfaces. SEM-EDX analysis confirms that Mo is uniformly distributed over the carbon matrix (see also Fig. S2†). HR-TEM, in Fig. 2b, indicates that the sample consists of opaque nanoparticles (~5 nm diameter), embedded within

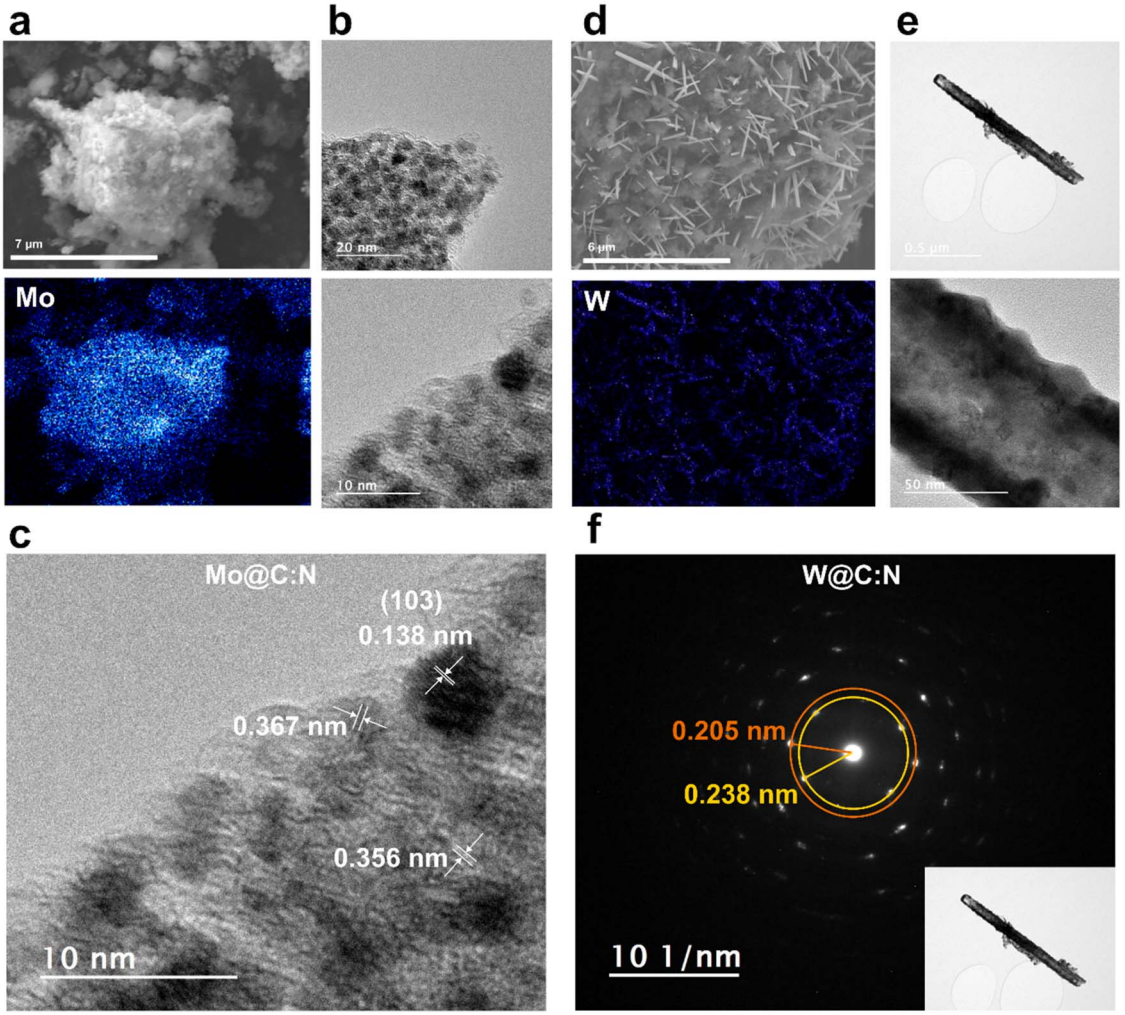

Fig. 2 SEM and EDX mapping (a) and HR-TEM (b) of Mo@C:N; (c) HR-TEM for Mo@C:N with measured *d*-spacings (white arrow). SEM and EDX mapping (d) and HR-TEM (e) of W@C:N; (f) SAED pattern of WN nanorods with estimated *d*-spacing.

a graphitised carbon matrix: nanoparticles exhibit lattice *d*-spacing of 0.138 nm, in Fig. 2c, closely matching (103) reflections of Mo_2C at 0.135 nm (PDF#35-0787). SEM of W@C:N, in Fig. 2d, displays a porous solid matrix with well-defined rod-like nanostructures with diameters in the 50–200 nm range. SEM-EDX indicates that these nanorods are rich in W (see also Fig. S2†). HR-TEM of such features, in Fig. 2e, reveals that they display well defined crystal facets and are encapsulated within a graphitised shell 10–20 nm in thickness. The selected area electron diffraction (SAED) pattern of nanorods, in Fig. 2f, confirms *d*-spacings of 0.238 nm and 0.205 nm, consistent with the (111) and (200) reflections of WN at 0.238 nm and 0.206 nm, respectively (PDF#65-2898).

Surface composition was studied using XPS and Table 2 summarises results obtained from best fits of high-resolution spectra for all materials. Survey spectra, Fig. S3,† display peaks associated with C 1s, N 1s and O 1s ionisations, as well as those associated with characteristic Mo and W ionisations for the respective M@C:N materials. Both the nitrogen and metal %-contents are much lower for W@C:N than for Mo@C:N, despite the two metals being present at similar atomic bulk concentrations. Indeed, a comparison between metal/carbon atomic %-ratios obtained by XPS and those from bulk determinations (Table 1) indicates that while W remains preferentially in the bulk, or below sub-surface, Mo is found predominantly at the air interface.

C 1s spectra of Mo@C:N and W@C:N are shown in Fig. 3a. The C 1s peak was deconvoluted using five components attributed to sp^2 (*ca.* 284.4 eV) and sp^3 (*ca.* 285.4 eV) carbon, C–O/C–N (*ca.* 287 eV) and C=O/COOH (*ca.* 289 eV) groups, and π–π^* excitations (*ca.* 292 eV).[50–53] For all materials, the sp^2 peak constitutes the largest contribution to the total intensity, as shown in Table 2 suggesting that materials undergo graphitisation to a similar extent during the annealing step. N 1s spectra are shown in Fig. S3;† the low N-content in W@C:N results in low overall intensity, nonetheless, peak binding energies at *ca.* 498 eV for both spectra suggest that pyridinic-N accounts for the majority of contributions, as was also observed for metal-free RPM/BP (Fig. S4†). Best-fits obtained using three components assigned to graphitic-N, pyrrolic-N and pyridinic-N,[51,54] with details summarised in Table S2,† support this conclusion. An additional peak at 394.6 eV is also observed for Mo@C:N and is characteristic of Mo $3p_{3/2}$ ionisations.[55–57] Finally, we note that differences in N/C surface content observed *via* XPS spectra are consistent with results from XRD characterization. XRD showed that annealing yields MoC_x/MoO_x and WN phases in Mo@C:N and W@C:N, respectively. This indicates that N-precursors react readily with W and are sequestered to the subsurface, as is the case for the W atoms, whereas for Mo@C:N they remain available to react with the carbon matrix.

The Mo 3d spectrum of Mo@C:N, Fig. 3b, was fitted using three doublets with an energy splitting of 3.1 eV, assigned to Mo^{2+} (228.5 eV), Mo^{4+} (229.8 eV), and Mo^{6+} (232.2 eV) species. Mo^{2+} components indicate the presence of molybdenum carbides in the form of Mo_2C and/or MoC, whereas Mo^{4+} and Mo^{6+} arise from oxide species due to surface oxidation in air, in agreement with previous reports for Mo carbides.[55,58,59] Peak area ratios indicate that the majority of surface Mo (>80%) is indeed oxidised after air exposure, in contrast with the predominance of carbide phases in the bulk, evidenced by XRD studies.

The W 4f spectrum of W@C:N, Fig. 3c, was fitted using two doublets with energy splitting of *ca.* 3 eV.[50,60–62] The $4f_{7/2}$ peak at low binding energy (32.2 eV) is characteristic of either W_2C or WN,[63–65] and therefore consistent with XRD results. The $4f_{7/2}$ peak at high binding energy (35.2 eV) is assigned to oxidised tungsten in the form of WO_3.[61,65] Notably, the oxide component accounts for a minority of surface W species, while carbides/nitrides constitute 64–68% of the contributions from metal centres. These compounds have been reported to oxidise in air as demonstrated by multiple studies,[58,66–69] therefore the absence of significant contributions from oxide species suggests that the majority of the carbide/nitride phases are encapsulated within a protective carbon shell that prevents/minimises oxidation.[13] This further supports findings from HR-TEM, while being consistent with the surface W-content being lower than the bulk value.

The electrochemical response was investigated *via* voltammetry experiments in 0.1 M H_2SO_4 using glassy carbon disks modified with the M@C:N materials *via* drop casting. Fig. 4 shows linear sweep voltammograms (LSV) for Mo@C:N and W@C:N at 2 mV s^{-1} in the presence and absence of 30.0 mM benzaldehyde in the electrolyte. In the absence of benzaldehyde, Mo@C:N displays HER activity ($\eta = -0.16$ V at 1.5 mA cm^{-2}) comparable to that observed at a range of Mo_2C electrodes under similar conditions.[59,70–72] The presence of a cathodic peak at −0.078 V, characteristic of proton-coupled reductions of MoO_3 at low pH,[72–74] is consistent with a significant concentration of Mo^{6+} at the electroactive surface of Mo@C:N and with evidence from XPS characterisation. Mo_2C is reported to be activated under cathodic polarisation,[72] while MoO_2/MoO_3 are sluggish in the HER;[72] therefore the observed

Table 2 Summary of atomic elemental compositions and selected best-fit results obtained from high resolution XPS spectra of synthesised materials

Material	C_{sp^2}/C_{tot}[a] (%)	N/C (at%)	M/C (at%)	MC_x or MN_x/M_{tot} (%)	$M-O/M_{tot}$ (at%)
Mo@C:N	63.4	19.5	5.7	16.3	83.7
W@C:N	57.4	1.7	0.45	64.3	35.7
RPM/BP	51.6	4.69	NA	NA	NA

[a] Calculated as area ratio of the best-fit component at 284.4 eV over the total C 1s peak.

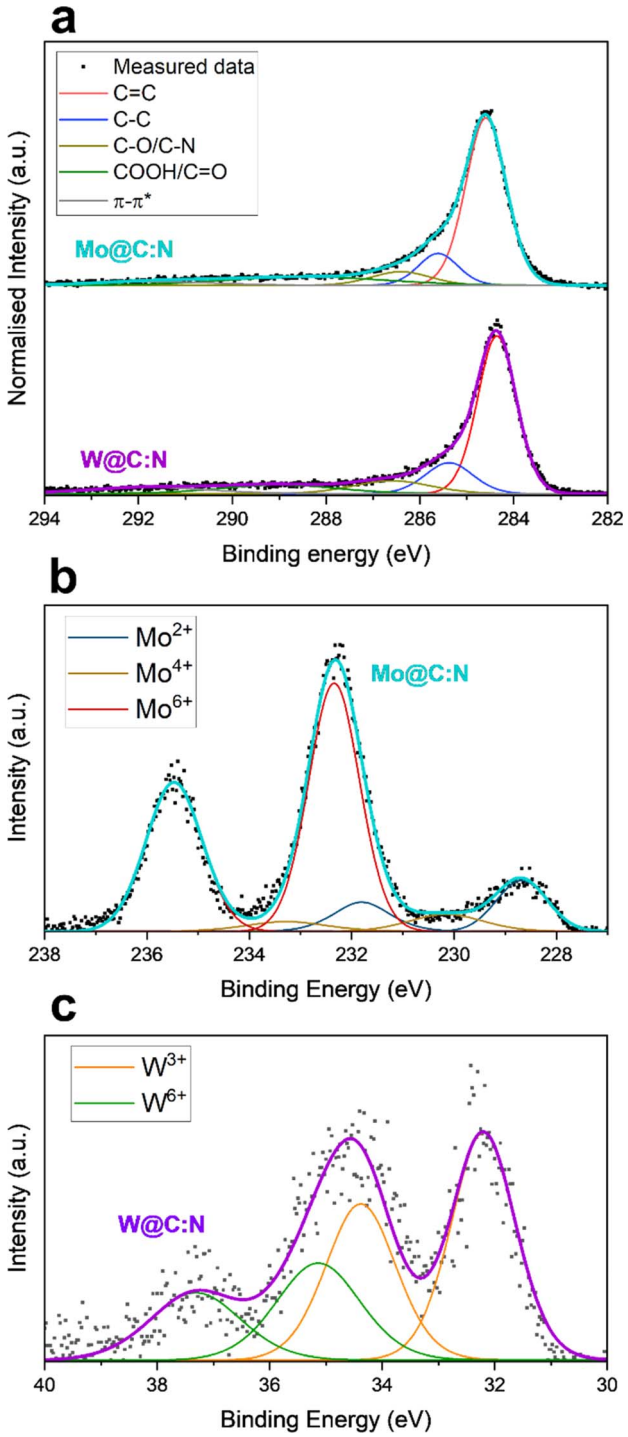

Fig. 3 (a) High resolution spectra and best-fits in the C 1s region for Mo@C:N (top) and W@C:N (bottom). High resolution spectra and best-fits in the (b) Mo 3d and (c) W 4f regions of Mo@C:N and W@C:N, respectively.

activity of Mo@C:N in acid electrolytes is likely to be dominated by Mo^{2+} centres at the electrolyte interface.

W@C:N also shows activity in the HER ($\eta = -0.50$ V at 1.5 mA cm^{-2}) but with lower current densities relative to Mo@C:N. Similar overpotentials have been reported for either WN[75] or carbon-encapsuled WC electrodes.[76] Interestingly, the LSV is

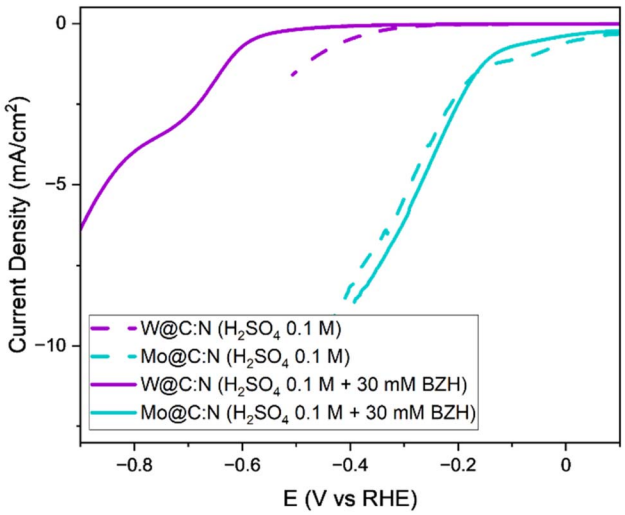

Fig. 4 LSV collected on GC disk for W@C:N and Mo@C:N in 0.1 M H_2SO_4 (dashed line) and 0.1 M H_2SO_4 with 30 mM BZH (solid line), at 2 mV s^{-1} scan rate.

devoid of peaks characteristic of proton-coupled reductions of WO_3 species,[77] thus supporting the conclusion from XPS that the majority of W surface sites are in a low oxidation state. Given that drop-cast films are porous, a comparison of the LSV curves was also carried out after normalisation by capacitive contributions to account for differences in microscopic area (Fig. S5†).[78–80] Mo@C:N was found to still display higher HER currents than W@C:N in agreement with prior reports of better HER performance in general for MoC_x *vs.* WC_x electrodes in acid electrolytes.[81] Finally, control LSV experiments with polished glassy carbon and metal-free RPM/BP electrodes, Fig. S5,† yielded higher HER overpotentials than either Mo@C:N or W@C:N after correction for microscopic area. Results, therefore, strongly suggest that M@C:N materials have improved intrinsic HER activity relative to metal-free graphitic carbons and that this can be attributed to the incorporation of Mo/W centres in the form of carbides/nitrides.

LSV in 0.1 M H_2SO_4 with 30 mM benzaldehyde at 2 mV s^{-1}, in Fig. 4, show a cathodic peak associated with the reduction of the organic at W@C:N (*ca.* −0.7 V), while the overall cathodic current density is decreased relative to the LSV in supporting electrolyte. This indicates a general quenching of HER faradaic currents due to adsorption of the organic species.[13,82,83] On the other hand, Mo@C:N displays only slight changes in current density while only a broad, ill-defined peak is discernible over the cathodic background current (*ca.* −0.3 V). This suggests that there is minimal competition by organic species for the HER-active sites at the Mo@C:N surface. Nonetheless, the peak at −0.078 V, visible in supporting electrolyte, is suppressed thus suggesting that benzaldehyde interacts with Mo^{6+} surface sites.

Benzaldehyde reactions were then studied using electrolysis experiments coupled to product detection. Carbon cloth (CC) current collectors were drop-coated using the same ink dispersions as for disk voltammetry studies. Fig. 5a and b show SEM and SEM-EDX images of CC coated with Mo@C:N and W@C:N,

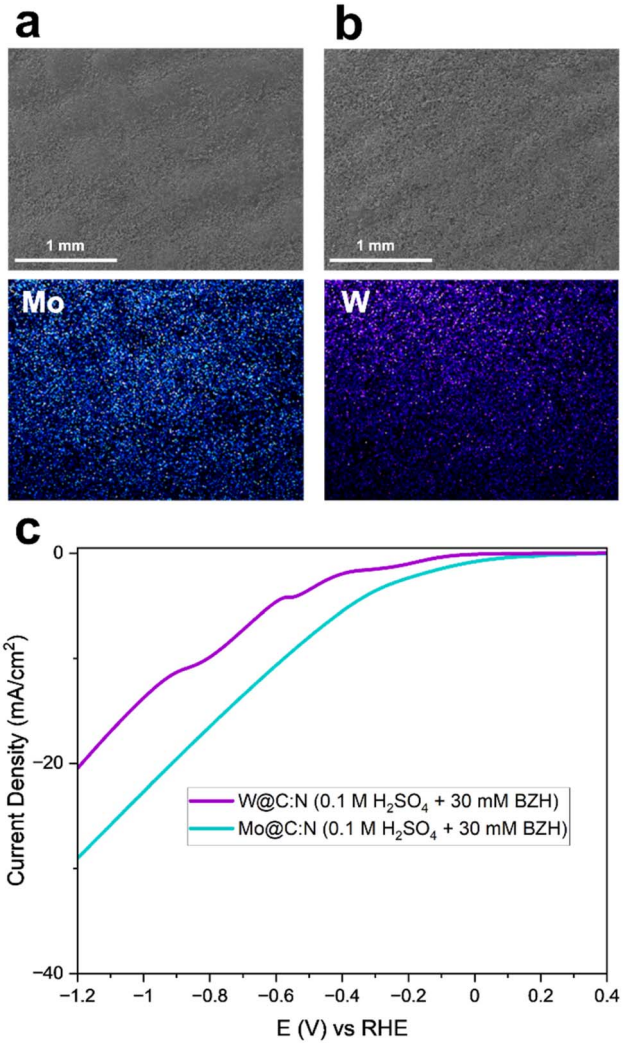

Fig. 5 SEM images and EDX mapping of CC electrodes coated with (a) Mo@C:N and (b)W@C:N electrocatalyst inks. (c) LSV collected for W@C:N and Mo@C:N on CC support in 0.1 M H_2SO_4 + 30 mM BZH. An expanded view over 0 to −0.9 V is shown in Fig. S8.†

respectively, indicating uniform metal distribution over the CC surface. The LSV in supporting electrolyte (Fig. S6†) shows that the presence of the carbon materials increases the capacitance of CC significantly, as expected after coating with a porous particle film. Capacitance values were found to be comparable for Mo@C:N and W@C:N (Fig. S7 and Table S3†), suggesting that the two materials do not differ significantly in ECSA despite their differences in BET area. Fig. 5c shows LSVs recorded for Mo@C:N and W@C:N on CC in 30 mM BZH in 0.1 M H_2SO_4. W@C:N displays multiple broad cathodic peaks between −0.8 and −0.26 V whereas Mo@C:N yields a featureless response, likely due to HER being the dominant contribution to the LSV, as observed for disk electrodes. The presence of multiple peaks associated with benzaldehyde in the LSV could arise from either mixed mass transport regimes in the porous CC electrode,[84,85] or from reduction at different functional sites, as observed by some even at carbon disk electrodes of well-defined geometry.[86]

An H-cell was used for electrolysis studies, as previously described.[13] Chronoamperometry experiments were carried out in a 30 mM BZH in 0.1 M H_2SO_4 solution at three selected potentials: −0.26, −0.5 and −0.8 V *vs.* RHE, as shown in Fig. 6a. Catalyst layers displayed high mechanical stability over the duration of the experiments thus yielding stable chronoamperogram curves (Fig. S9†). Repeat potential step experiments also yielded comparable chronoamperograms (Fig. S9†), thus confirming the robustness and stability of the fabricated electrodes. Log–log plots of current *vs.* time (Fig. S9†) show that after *ca.* 100–150 s, the slope of these plots transitions from a value of *ca.* −0.5 to a value close to zero, indicative of convective control. Evidence of convection is in agreement with prior work on similar electrode materials and is attributed to gas evolution during HER.[13]

Both benzyl alcohol (BA) and hydrobenzoin (HBZ) were identified as reduction products *via* gas chromatography, confirming the hydrogenation of benzaldehyde. Carbon balance was found to be *ca.* 90% (Fig. S10†) for all materials, indicating negligible mass losses due to diffusion through the membrane, loss to the headspace and/or to surface adsorption. Yields and conversion values were calculated for all materials and are shown in Fig. S11.† As the potential is shifted to more cathodic values, both conversion and yield show an increase, while the preferred product remains BA (Fig. S12†). At any given potential, better yields and conversions were observed for W@C:N *vs.* Mo@C:N over 2 h, thus suggesting that given, the same metal atomic concentrations, W-containing catalyst layers result in better operational performances in organic hydrogenations.

The faradaic efficiency, FE_{ECH} were calculated and are summarised in Fig. 6b. Mo@C:N shows good FE_{ECH} at the lowest overpotential, but the efficiency of reductions decreases significantly at −0.5 V before increasing slightly at −0.8 V again. The greater HER activity of Mo@C:N *vs.* W@C:N and RPM/BP, enables facile H_{ads} activation even at −0.26 V which increases rates of ECH *via* H_{ads} addition or concerted e-H^+ additions;[5,82] however, as the potential is shifted to more cathodic values, the HER becomes the dominant faradaic process decreasing the overall efficiency of ECH. At higher cathodic overpotentials proton coupled reductions of BZH can become an additional and energetically favourable pathway for the production of BA/HBZ particularly at carbon surfaces, as discussed in detail in computational studies by Cantu *et al.*[5] We believe this is likely to explain the increase in FE_{ECH} at −0.8 V for Mo@C:N. In the case of both W@C:N and RPM/BP, the efficiencies are low at −0.26 V but superior to that of Mo@C:N at −0.5 V, which is consistent with these materials being less effective at evolving hydrogen and with the HER being suppressed as a competing reaction at −0.5 V.

Product rates normalised by geometric area and by capacitance are shown in Fig. 6c and d, respectively. Normalisation by capacitance puts in clear evidence the significant differences in specific electroactive area between the metal-free material and M@C:N catalysts, as well as the superior performance in organic hydrogenations obtained with the latter. W@C:N materials offer significant advantages at −0.5 and −0.8 V. Interestingly, while the Volmer step is facile and H_2 desorption

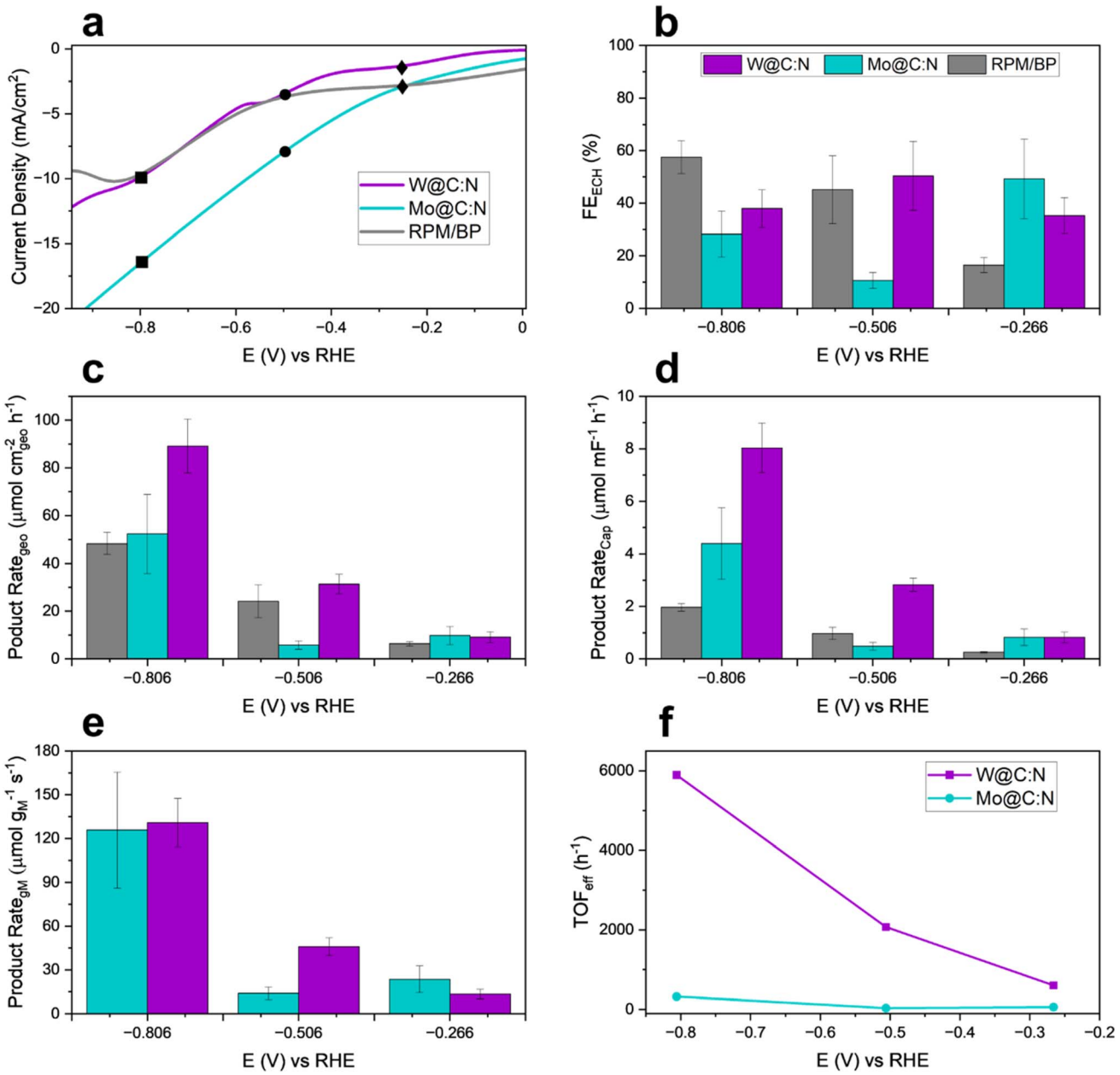

Fig. 6 (a) LSV collected for W@C:N and Mo@C:N on CC support in 0.1 M H_2SO_4 + 30 mM BZH with highlighted potential at −0.26 V (◆), −0.5 V (●) and −0.8 V (■) *vs.* RHE. (b) Total ECH FE %. Product rate normalised by geometric area (c), by capacitance (d), and by amount of metal in the bulk for both M@C:N (e). TOF calculated values for both M@C:N samples normalised for surface atomic concentrations (f).

limiting at WC/WN,[24,87] it is H_{ads} activation that is rate determining at carbons. Therefore, H_{ads} coverages should remain low at RPM/BP but increase readily with cathodic overpotential at WN, which likely explains why the product rate normalised by specific area is markedly superior for W@C:N at both −0.5 V and −0.8 V.

Fig. 6e shows product rates for Mo@C:N and W@C:N after normalisation by bulk metal contents. These results align with trends in FE_{ECH}, showing higher performance for Mo@C:N at −0.26 V and for W@C:N at −0.5 V; while at −0.8 V the two material shows similar product rates. However, their performances diverge when considering differences in surface segregation between Mo and W centres observed for the two M@C:N. This can be taken into account by estimating an effective turnover frequency (TOF_{eff}) for W and Mo metal centres at the electrolyte interface. Assuming that the double-layer capacitance arises from the carbon matrix alone (20 μF cm^{-2})[88,89] and accounting for the areal carbon density of graphite of 3.82×10^{15} atoms per cm^2,[90] TOF_{eff} values can be calculated using the atomic %-contents of 0.43% and 4.3% for W and Mo, respectively, obtained from XPS. TOF_{eff} values thus calculated are shown in Fig. 6f and suggest that encapsulated W centers yield significant advantages in terms of intrinsic activity.

The above results indicate that both Mo@C:N and W@C:N show activity in the hydrogenation of benzaldehyde and that W@C:N appears to be particularly promising, achieving satisfactory FE_{ECH} and good product rates at moderate potentials. At low overpotentials, FE_{ECH} values for Mo@C:N samples are comparable to those reported for Pt/C (~60%) and exceed those of similar M@C:N architectures synthesised using Fe as a metal core.[13,82] Further, W@C:N shows good FE_{ECH} at −0.5 V compared to Pt/C, as determined by Song *et al.* at pH 5 and similar potentials.[82] Interestingly, TOF_{eff} values estimated for W@C:N under our operational conditions are comparable to those reported for Pt/C and Rh/C catalysts at −0.5 V *vs.* RHE in the same work. Additionally, both M@C:N materials show high TOF values relative to our previous report using Fe@C:N.[13] Our findings therefore suggest that compositional changes can be successfully leveraged to modulate and improve ECH performance at M@C architectures based on transition metals.

It is important however to highlight that, when interpreting differences in performance between Mo and W-containing electrodes it remains challenging to disentangle the effects of a change in metal identity (W *vs.* Mo), from those arising from morphological and compositional differences that result from metal-catalysed graphitisation. In the case of W@C:N materials, metal centres are encapsulated and protected from oxidation; the majority of them are present in the form of WN nanorods that can improve, simultaneously, H_{ads} stabilisation[24,87] and metallic character/conductivity of the porous carbon matrix. For Mo@C:N it is also possible to argue that H_{ads} coverages are stabilised relative to RPM/BP; however, the presence of surface MoO_x indicates that only a fraction of metal sites should facilitate H_{ads} activation, while charge transfer impedances are likely to be negatively affected by surface oxidised phases.[91]

Finally, the calculation of TOF_{eff} values assumes implicitly that the metal sites are responsible for BZH reduction rates. This is likely an oversimplification that neglects possible activation of multiple N-/C-sites due to *e.g.* proximity effects of metal in the sub-surface,[18,20] as well as the fact that hydrogenation pathways are potential-dependent.[5] First, several proposed hypotheses have been put forward to explain the nature of the active site at M@C:N electrodes in the HER. Both M-sites in contact with the electrolyte but with their reactivity modulated by the surrounding carbon matrix, or C/N-sites with their reactivity modulated by metals in the subsurface are considered as possible and experimentally consistent explanations for H_{ads} activation at carbon-encapsulated architectures. However, unequivocal identification of these active sites remains a topic of ongoing debate, as highlighted recently by Yoo *et al.*,[92] despite the HER being a considerably simpler reaction than the ECH of benzaldehyde. Nonetheless, and regardless of whether the active sites are C- or M-centers, the activity remains dependent on the degree to which the metal is in proximity to, or at, the surface. Therefore, XPS atomic coverages, which reflect metal content within the first 1–3 nm from the surface, are a relevant quantity when attempting to account for metal effects on surface reactivity. A more in-depth analysis of the active site in the ECH is likely to require further experimental work, including *e.g.* use of poisoning/capping agents.[92] Second, potential-dependence of the active site must also be contemplated; at increasing cathodic overpotentials it is reasonable to assume that the total product rate stems at least in part from proton coupled reductions, as noted when discussing FE_{ECH} values at −0.8 V. Indeed, contributions from M-site mediated H-addition and from proton coupled reduction of BZH_{ads} must both be considered, particularly at high overpotentials and based on the current mechanistic understanding of ECH.[5,93–95] Therefore, the validity of assumptions underpinning TOF_{eff} calculations might be limited at the most negative potentials tested and comparisons between metal TOF values are best restricted to the low overpotential range where metal catalysed pathways are expected to dominate hydrogenation rates. Finally, although electrolysis experiments are performed in this work under natural convection and in an H-cell, well-defined convective conditions *e.g.* flow through electrolyser devices, would be desirable to fully account for mass transport effects, support comparative performance studies and investigate stability under conditions closer to those encountered in electrolyser applications.[20]

4. Conclusions

In this work we have investigated M@C:N architectures as a promising approach for developing materials that are active in the electrocatalytic hydrogenation of benzaldehyde. Building on encouraging results that demonstrated activity with low-cost metals such as Fe,[13] we show that the type of metal centre in M@C:N structures can be leveraged to regulate ECH performances, as observed by the significant enhancements in effective TOF resulting from a replacement of Mo with W centres.

The synthesis and properties of materials Mo@C:N and W@C:N, with nearly identical atomic metal contents of *ca.* 1.5%, were investigated. Structural characterisation revealed that Mo@C:N has a bulk composition primarily consisting of Mo_2C, but its surface is rich in oxides. In contrast, W@C:N has a bulk structure consisting of WN with minimal oxide present at its surface; W is localised in rod-like nanostructures protected from oxidation and likely corrosion by a graphitised shell. Both materials were found to be porous: the presence of W centres introduces only small changes in carbon porosity relative to the metal-free analogue material, whereas Mo centres catalyse pore opening.

Incorporation of Mo and W centres improves the HER activity for both materials compared to the metal free analogue RPM/BP, with Mo@C:N displaying higher HER cathodic currents. Electrolysis experiments coupled with gas chromatography analysis of products demonstrated that this translates into increased ECH activity at low overpotentials in the hydrogenation of benzaldehyde, the unsaturated compound used as a diagnostic substrate. Selectivity for the benzyl alcohol product was observed at all tested potentials; this is a promising result as achieving selectivity remains a challenge for most studied electrocatalysts, particularly at cathodic potentials.[13,82,83] Mo@C:N shows high FE at anodic potentials, while W@C:N is more efficient at cathodic potentials due to suppressed competition between HER and ECH pathways. Product rates

and TOF_{eff} values were used as a basis for comparison, with W@C:N showing higher ECH performances at the investigated atomic loading, especially when considering the differences in surface excess between the two metals. Estimated TOF_{eff} are comparable to those for Rh/C and Pt/C catalysts;[82] given the four orders of magnitude difference in material cost, results suggests that W@C:N architectures are likely to be cost-competitive for ECH applications and could reduce pressure on precious and critical raw materials for ECH implementation at scale.

Data availability

Data for this article, including X-ray diffraction (XRD), isotherms and pore size distributions, X-ray photoelectron spectroscopy (XPS), Scanning electron microscopy (SEM), cyclic and linear sweep voltammetry (CV and LSV), electrolysis raw data at different conditions of organic concentration and potential, Faradic efficiency (FE), product rates, turn over frequency (TOF), and transmission electron microscopy (TEM), are available at Trinity's Access to Research Archive (TARA) at **https://hdl.handle.net/2262/110448**.

Conflicts of interest

There are no conflicts of interest to declare.

Acknowledgements

This publication has emanated from research conducted with the financial support of Taighde Éireann – Research Ireland under Grant number 19/FFP/6761 and GOIPD/2021/530. PEC, FB and JAB thank the France-Ireland PHC ULYSSES 2021 programme for supporting part of the work. SEM imaging was carried out at the Advanced Microscopy Laboratory (AML) at the AMBER Research Centre, Trinity College Dublin, Ireland. We acknowledge kind support from the Earth Surface Research Laboratory for access to ED-XRF. We are grateful to the THEMIS platform (ScanMAT) at the Université de Rennes for support with HR-TEM. Use of the XPS of I. V. Shvets and C. McGuinness provided under SFI Equipment Infrastructure funds.

References

1 G. Zhao, K. Rui, S. X. Dou and W. Sun, Heterostructures for Electrochemical Hydrogen Evolution Reaction: A Review, *Adv. Funct. Mater.*, 2018, **28**, 1803291.
2 S. A. Akhade, N. Singh, O. Y. Gutiérrez, J. Lopez-Ruiz, H. Wang, J. D. Holladay, Y. Liu, A. Karkamkar, R. S. Weber, A. B. Padmaperuma, M.-S. Lee, G. A. Whyatt, M. Elliott, J. E. Holladay, J. L. Male, J. A. Lercher, R. Rousseau and V.-A. Glezakou, Electrocatalytic hydrogenation of biomass-derived organics: a review, *Chem. Rev.*, 2020, **120**, 11370–11419.
3 Y. Zeng, M. Zhao, H. Zeng, Q. Jiang, F. Ming, K. Xi, Z. Wang and H. Liang, Recent progress in advanced catalysts for electrocatalytic hydrogenation of organics in aqueous conditions, *eScience*, 2023, **3**, 100156.
4 L. Zhang, T. U. Rao, J. Wang, D. Ren, S. Sirisommboonchai, C. Choi, H. Machida, Z. Huo and K. Norinaga, A review of thermal catalytic and electrochemical hydrogenation approaches for converting biomass-derived compounds to high-value chemicals and fuels, *Fuel Process. Technol.*, 2022, **226**, 107097.
5 D. C. Cantu, A. B. Padmaperuma, M.-T. Nguyen, S. A. Akhade, Y. Yoon, Y.-G. Wang, M.-S. Lee, V.-A. Glezakou, R. Rousseau and M. A. Lilga, A combined experimental and theoretical study on the activity and selectivity of the electrocatalytic hydrogenation of aldehydes, *ACS Catal.*, 2018, **8**, 7645–7658.
6 J. Anibal, A. Malkani and B. Xu, Stability of the ketyl radical as a descriptor in the electrochemical coupling of benzaldehyde, *Catal. Sci. Technol.*, 2020, **10**, 3181–3194.
7 E. Andrews, J. A. Lopez-Ruiz, J. D. Egbert, K. Koh, U. Sanyal, M. Song, D. Li, A. J. Karkamkar, M. A. Derewinski, J. Holladay, O. Y. Gutiérrez and J. D. Holladay, Performance of base and noble metals for electrocatalytic hydrogenation of bio-oil-derived oxygenated compounds, *ACS Sustainable Chem. Eng.*, 2020, **8**, 4407–4418.
8 K. Amouzegar and O. Savadogo, Electrocatalytic hydrogenation of phenol on dispersed Pt: reaction mechanism and support effect, *Electrochim. Acta*, 1998, **43**, 503–508.
9 S. J. C. Cleghorn and D. Pletcher, The mechanism of electrocatalytic hydrogenation of organic molecules at palladium black cathodes, *Electrochim. Acta*, 1993, **38**, 425–430.
10 Z. Li, S. Kelkar, L. Raycraft, M. Garedew, J. E. Jackson, D. J. Miller and C. M. Saffron, A mild approach for bio-oil stabilization and upgrading: electrocatalytic hydrogenation using ruthenium supported on activated carbon cloth, *Green Chem.*, 2014, **16**, 844–852.
11 B. zhao, M. Chen, Q. Guo and Y. Fu, Electrocatalytic hydrogenation of furfural to furfuryl alcohol using platinum supported on activated carbon fibers, *Electrochim. Acta*, 2014, **135**, 139–146.
12 **https://www.dailymetalprice.com**and **https://www.metal.com/**, accessed 10, December, 2024.
13 F. Pota, M. Costa de Oliveira, C. Schröder, M. Brunet Cabré, H. Nolan, A. Rafferty, O. Jeannin, F. Camerel, J. Behan, F. Barrière and P. E. Colavita, Porous N-doped carbon-encapsulated iron as a novel catalyst architecture for the electrocatalytic hydrogenation of benzaldehyde, *ChemSusChem*, 2025, **18**, e202400546.
14 M. Tavakkoli, T. Kallio, O. Reynaud, A. G. Nasibulin, C. Johans, J. Sainio, H. Jiang, E. I. Kauppinen and K. Laasonen, Single-shell carbon-encapsulated iron nanoparticles: synthesis and high electrocatalytic activity for hydrogen evolution reaction, *Angew. Chem., Int. Ed.*, 2015, **54**, 4535–4538.
15 J. Deng, P. Ren, D. Deng and X. Bao, Enhanced electron penetration through an ultrathin graphene layer for highly efficient catalysis of the hydrogen evolution reaction, *Angew. Chem., Int. Ed.*, 2015, **54**, 2100–2104.

16 H. Wei, J. Wang, Q. Lin, Y. Zou, X. a. Chen, H. Zhao, J. Li, H. Jin, Y. Lei and S. Wang, Incorporating ultra-small N-doped Mo2C nanoparticles onto 3D N-doped flower-like carbon nanospheres for robust electrocatalytic hydrogen evolution, *Nano Energy*, 2021, **86**, 106047.
17 N. Han, K. R. Yang, Z. Lu, Y. Li, W. Xu, T. Gao, Z. Cai, Y. Zhang, V. S. Batista, W. Liu and X. Sun, Nitrogen-doped tungsten carbide nanoarray as an efficient bifunctional electrocatalyst for water splitting in acid, *Nat. Commun.*, 2018, **9**, 924.
18 Y. Peng and S. Chen, Electrocatalysts based on metal@carbon core@shell nanocomposites: an overview, *Green Energy Environ.*, 2018, **3**, 335–351.
19 C. Gao, F. Lyu and Y. Yin, Encapsulated metal nanoparticles for catalysis, *Chem. Rev.*, 2021, **121**, 834–881.
20 L. Zhang, J. Xiao, H. Wang and M. Shao, Carbon-based electrocatalysts for hydrogen and oxygen evolution reactions, *ACS Catal.*, 2017, **7**, 7855–7865.
21 W. Wan, S. Wei, J. Li, C. A. Triana, Y. Zhou and G. R. Patzke, Transition metal electrocatalysts encapsulated into N-doped carbon nanotubes on reduced graphene oxide nanosheets: efficient water splitting through synergistic effects, *J. Mater. Chem. A*, 2019, **7**, 15145–15155.
22 J. Lessard, Electrocatalytic hydrogenation, in *Encyclopedia of Applied Electrochemistry*, 2014, pp. 443–448.
23 S. Trasatti, Work function, electronegativity, and electrochemical behaviour of metals: III. Electrolytic hydrogen evolution in acid solutions, *J. Electroanal. Chem. Interfacial Electrochem.*, 1972, **39**, 163–184.
24 R. Michalsky, Y.-J. Zhang and A. A. Peterson, Trends in the hydrogen evolution activity of metal carbide catalysts, *ACS Catal.*, 2014, **4**, 1274–1278.
25 A. G. Mitchell and L. S. C. Wan, Oxidation of aldehydes solubilized in nonionic surfactants I: solubility of benzaldehyde and methylbenzaldehyde in aqueous solutions of polyoxyethylene glycol ethers, *J. Pharm. Sci.*, 1964, **53**, 1467–1470.
26 O. Hammerich and B. Speiser, *Organic Electrochemistry*, CRC press, Boca Raton, 2016.
27 Y. Ran, J. Li, J. Sun, B. Yu, F. Tan, G. Cheng and Z. Zhang, Impact of alloying on electrocatalytic hydrogenation of benzaldehyde over sputtered NiCu film catalysts, *Appl. Catal., A*, 2024, **678**, 119725.
28 G. Cheng, J. Sun, Y. Ran, F. Tan, W. Ma and Z. Zhang, Effective free-standing electrodes with refined structure *via* sputtering Ti sublayer and altering working pressure for electrocatalytic benzaldehyde hydrogenation, *Chem. Eng. J.*, 2024, **481**, 148735.
29 L. Gong, C. Y. Zhang, J. Li, G. Montaña-Mora, M. Botifoll, T. Guo, J. Arbiol, J. Y. Zhou, T. Kallio, P. R. Martínez-Alanis and A. Cabot, Enhanced electrochemical hydrogenation of benzaldehyde to benzyl alcohol on Pd@Ni-MOF by modifying the adsorption configuration, *ACS Appl. Mater. Interfaces*, 2024, **16**, 6948–6957.
30 C.-C. Liu, A. B. Walters and M. A. Vannice, Measurement of electrical properties of a carbon black, *Carbon*, 1995, **33**, 1699–1708.
31 M. Carmo, A. R. dos Santos, J. G. R. Poco and M. Linardi, Physical and electrochemical evaluation of commercial carbon black as electrocatalysts supports for DMFC applications, *J. Power Sources*, 2007, **173**, 860–866.
32 S. Brunauer, P. H. Emmett and E. Teller, Adsorption of gases in multimolecular layers, *J. Am. Chem. Soc.*, 1938, **60**, 309–319.
33 J. Rouquerol, P. Llewellyn and F. Rouquerol, Is the BET equation applicable to microporous adsorbents?, in *Studies in Surface Science and Catalysis*, Elsevier, 2007, vol. 160, pp. 49–56.
34 V. Fierro, G. Bosch and F. R. Siperstein, Pore size distribution in microporous carbons obtained from molecular modeling and density functional theory, in *Studies in Surface Science and Catalysis*, ed. P. L. Llewellyn, F. Rodriquez-Reinoso, J. Rouqerol and N. Seaton, Elsevier, 2007, vol. 160, pp. 519–526.
35 G. Kupgan, T. P. Liyana-Arachchi and C. M. Colina, NLDFT pore size distribution in amorphous microporous materials, *Langmuir*, 2017, **33**, 11138–11145.
36 J. A. Behan, A. Iannaci, C. Domínguez, S. N. Stamatin, M. K. Hoque, J. M. Vasconcelos, T. S. Perova and P. E. Colavita, Electrocatalysis of N-doped carbons in the oxygen reduction reaction as a function of pH: N-sites and scaffold effects, *Carbon*, 2019, **148**, 224–230.
37 A. Iannaci, S. Ingle, C. Domínguez, M. Longhi, O. Merdrignac-Conanec, S. Ababou-Girard, F. Barrière and P. E. Colavita, Nanoscaffold effects on the performance of air-cathodes for microbial fuel cells: sustainable Fe/N-carbon electrocatalysts for the oxygen reduction reaction under neutral pH conditions, *Bioelectrochemistry*, 2021, **142**, 107937.
38 M. Karthik, A. Faik, S. Doppiu, V. Roddatis and B. D'Aguanno, A simple approach for fabrication of interconnected graphitized macroporous carbon foam with uniform mesopore walls by using hydrothermal method, *Carbon*, 2015, **87**, 434–443.
39 M. Zhang, Y. Qiu, Y. Han, Y. Guo and F. Cheng, Three-dimensional tungsten nitride nanowires as high performance anode material for lithium ion batteries, *J. Power Sources*, 2016, **322**, 163–168.
40 L. Shen and N. Wang, Effect of nitrogen pressure on the structure of Cr-N, Ta-N, Mo-N, and W-N nanocrystals synthesized by Arc discharge, *J. Nanomater.*, 2011, **2011**, 781935.
41 K. S. W. Sing, Reporting physisorption data for gas/solid systems with special reference to the determination of surface area and porosity (Recommendations 1984), *Pure Appl. Chem.*, 1985, **57**, 603–619.
42 M. Thommes, K. Kaneko, A. V. Neimark, J. P. Olivier, F. Rodriguez-Reinoso, J. Rouquerol and K. S. W. Sing, Physisorption of gases, with special reference to the evaluation of surface area and pore size distribution (IUPAC Technical Report), *Pure Appl. Chem.*, 2015, **87**, 1051–1069.
43 R. T. K. Baker, J. J. Chludzinski, N. C. Dispenziere and L. L. Murrell, Catalytic gasification of graphite by:

tungsten, rhenium, and tungsten-rhenium, *Carbon*, 1983, **21**, 579–588.
44 T. Wang, J. Tang, X. Fan, J. Zhou, H. Xue, H. Guo and J. He, The oriented growth of tungsten oxide in ordered mesoporous carbon and their electrochemical performance, *Nanoscale*, 2014, **6**, 5359–5371.
45 J. Li, Z. Zhang, Z. Wang, Q. Cao, F. Guo and Q. Cao, Low temperature graphitization and electrochemical properties of porous carbon catalyzed with bimetal Ni-Mo, *Diamond Relat. Mater.*, 2022, **123**, 108862.
46 H. Guo, Y. Song, P. Chen, H. Lou and X. Zheng, Effects of graphitization of carbon nanospheres on hydrodeoxygenation activity of molybdenum carbide, *Catal. Sci. Technol.*, 2018, **8**, 4199–4208.
47 A. Ōya and S. Ōtani, Catalytic graphitization of carbons by various metals, *Carbon*, 1979, **17**, 131–137.
48 S. Braun, L. G. Appel and M. Schmal, Molybdenum species on alumina and silica supports for soot combustion, *Catal. Commun.*, 2005, **6**, 7–12.
49 J. P. A. Neeft, M. Makkee and J. A. Moulijn, Catalysts for the oxidation of soot from diesel exhaust gases. I. An exploratory study, *Appl. Catal., B*, 1996, **8**, 57–78.
50 J. Chastain and R. C. King Jr, *Handbook of X-Ray Photoelectron Spectroscopy*, Perkin-Elmer Corporation, 1992, 40, p. 221.
51 N. Hellgren, R. T. Haasch, S. Schmidt, L. Hultman and I. Petrov, Interpretation of X-ray photoelectron spectra of carbon-nitride thin films: new insights from *in situ* XPS, *Carbon*, 2016, **108**, 242–252.
52 L. Qu, Y. Liu, J.-B. Baek and L. Dai, Nitrogen-doped graphene as efficient metal-free electrocatalyst for oxygen reduction in fuel cells, *ACS Nano*, 2010, **4**, 1321–1326.
53 J. T. Titantah and D. Lamoen, Carbon and nitrogen 1s energy levels in amorphous carbon nitride systems: XPS interpretation using first-principles, *Diamond Relat. Mater.*, 2007, **16**, 581–588.
54 M. A. Costa de Oliveira, C. Schröder, M. Brunet Cabré, H. Nolan, A. Forner-Cuenca, T. S. Perova, K. McKelvey and P. E. Colavita, Effects of N-functional groups on the electron transfer kinetics of VO^{2+}/VO_2^+ at carbon: decoupling morphology from chemical effects using model systems, *Electrochim. Acta*, 2024, **475**, 143640.
55 Y.-Y. Chen, Y. Zhang, W.-J. Jiang, X. Zhang, Z. Dai, L.-J. Wan and J.-S. Hu, Pomegranate-like N,P-doped Mo_2C@C nanospheres as highly active electrocatalysts for alkaline hydrogen evolution, *ACS Nano*, 2016, **10**, 8851–8860.
56 H. Wei, Q. Xi, X. a. Chen, D. Guo, F. Ding, Z. Yang, S. Wang, J. Li and S. Huang, Molybdenum carbide nanoparticles coated into the graphene wrapping N-doped porous carbon microspheres for highly efficient electrocatalytic hydrogen evolution both in acidic and alkaline media, *Adv. Sci.*, 2018, **5**, 1700733.
57 X. Yang, X. Feng, H. Tan, H. Zang, X. Wang, Y. Wang, E. Wang and Y. Li, N-doped graphene-coated molybdenum carbide nanoparticles as highly efficient electrocatalysts for the hydrogen evolution reaction, *J. Mater. Chem. A*, 2016, **4**, 3947–3954.
58 H. Preiss, B. Meyer and C. Olschewski, Preparation of molybdenum and tungsten carbides from solution derived precursors, *J. Mater. Sci.*, 1998, **33**, 713–722.
59 N. Malone, H. Fiedler, D. R. G. Mitchell, J. V. Kennedy, G. I. N. Waterhouse and P. Gupta, High turnover frequency for the hydrogen evolution reaction on molybdenum carbide thin films synthesized by ion implantation, *ACS Appl. Eng. Mater.*, 2023, **1**, 2377–2385.
60 C. C. Baker and S. I. Shah, Reactive sputter deposition of tungsten nitride thin films, *J. Vac. Sci. Technol. A*, 2002, **20**, 1699–1703.
61 Z. Wang, Z. Liu, Z. Yang and S. Shingubara, Characterization of sputtered tungsten nitride film and its application to Cu electroless plating, *Microelectron. Eng.*, 2008, **85**, 395–400.
62 Y. G. Shen, Y. W. Mai, D. R. McKenzie, Q. C. Zhang, W. D. McFall and W. E. McBride, Composition, residual stress, and structural properties of thin tungsten nitride films deposited by reactive magnetron sputtering, *J. Appl. Phys.*, 2000, **88**, 1380–1388.
63 S. Ouendi, K. Robert, D. Stievenard, T. Brousse, P. Roussel and C. Lethien, Sputtered tungsten nitride films as pseudocapacitive electrode for on chip micro-supercapacitors, *Energy Storage Mater.*, 2019, **20**, 243–252.
64 P. V. Krasovskii, O. S. Malinovskaya, A. V. Samokhin, Y. V. Blagoveshchenskiy, V. A. Kazakov and A. A. Ashmarin, XPS study of surface chemistry of tungsten carbides nanopowders produced through DC thermal plasma/hydrogen annealing process, *Appl. Surf. Sci.*, 2015, **339**, 46–54.
65 C. B. Rodella, D. H. Barrett, S. F. Moya, S. J. A. Figueroa, M. T. B. Pimenta, A. A. S. Curvelo and V. Teixeira da Silva, Physical and chemical studies of tungsten carbide catalysts: effects of Ni promotion and sulphonated carbon, *RSC Adv.*, 2015, **5**, 23874–23885.
66 A. S. Kurlov and A. I. Gusev, Oxidation of tungsten carbide powders in air, *Int. J. Refract. Met. Hard Mater.*, 2013, **41**, 300–307.
67 R. F. Voitovich and É. A. Pugach, High-temperature oxidation characteristics of the carbides of the Group VI transition metals, *Powder Metall. Met. Ceram.*, 1973, **12**, 314–318.
68 X. Huang, J. Wang, H. Bing Tao, H. Tian, Z. Zhang and H. Xu, Unraveling the oxide layer on Mo2C as the active center for hydrogen evolution reaction, *J. Catal.*, 2020, **389**, 461–467.
69 D. V. Esposito and J. G. Chen, Monolayer platinum supported on tungsten carbides as low-cost electrocatalysts: opportunities and limitations, *Energy Environ. Sci.*, 2011, **4**, 3900–3912.
70 B. Deng, Z. Wang, W. Chen, J. T. Li, D. X. Luong, R. A. Carter, G. Gao, B. I. Yakobson, Y. Zhao and J. M. Tour, Phase controlled synthesis of transition metal carbide nanocrystals by ultrafast flash Joule heating, *Nat. Commun.*, 2022, **13**, 262.
71 C. Wan, Y. N. Regmi and B. M. Leonard, Multiple phases of molybdenum carbide as electrocatalysts for the hydrogen evolution reaction, *Angew. Chem., Int. Ed.*, 2014, **53**, 6407–6410.

72 H. Vrubel and X. Hu, Molybdenum boride and carbide catalyze hydrogen evolution in both acidic and basic solutions, *Angew. Chem., Int. Ed.*, 2012, **51**, 12703–12706.
73 V. S. Saji and C.-W. Lee, Molybdenum, molybdenum oxides, and their electrochemistry, *ChemSusChem*, 2012, **5**, 1146–1161.
74 X. Wang, Y. Xie, K. Tang, C. Wang and C. Yan, Redox chemistry of molybdenum trioxide for ultrafast hydrogen-ion storage, *Angew. Chem., Int. Ed.*, 2018, **57**, 11569–11573.
75 S. R. Denny, B. M. Tackett, D. Tian, K. Sasaki and J. G. Chen, Exploring electrocatalytic stability and activity of unmodified and platinum-modified tungsten and niobium nitrides, *Int. J. Hydrogen Energy*, 2020, **45**, 22883–22892.
76 Y. C. Kimmel, D. V. Esposito, R. W. Birkmire and J. G. Chen, Effect of surface carbon on the hydrogen evolution reactivity of tungsten carbide (WC) and Pt-modified WC electrocatalysts, *Int. J. Hydrogen Energy*, 2012, **37**, 3019–3024.
77 M. A. Spencer, N. P. Holzapfel, K.-E. You, G. Mpourmpakis and V. Augustyn, Participation of electrochemically inserted protons in the hydrogen evolution reaction on tungsten oxides, *Chem. Sci.*, 2024, **15**, 5385–5402.
78 H. Nolan, C. Schröder, M. Brunet-Cabré, F. Pota, N. McEvoy, K. McKelvey, T. S. Perova and P. E. Colavita, MoS_2/carbon heterostructured catalysts for the hydrogen evolution reaction: N-doping modulation of substrate effects in acid and alkaline electrolytes, *Carbon*, 2023, **202**, 70–80.
79 S. I. Perez Bakovic, P. Acharya, M. Watkins, H. Thornton, S. Hou and L. F. Greenlee, Electrochemically active surface area controls HER activity for Fe_xNi_{100-x} films in alkaline electrolyte, *J. Catal.*, 2021, **394**, 104–112.
80 J. Kibsgaard, Z. Chen, B. N. Reinecke and T. F. Jaramillo, Engineering the surface structure of MoS_2 to preferentially expose active edge sites for electrocatalysis, *Nat. Mater.*, 2012, **11**, 963–969.
81 S. Hussain, D. Vikraman, A. Feroze, W. Song, K.-S. An, H.-S. Kim, S.-H. Chun and J. Jung, Synthesis of Mo_2C and W_2C nanoparticle electrocatalysts for the efficient hydrogen evolution reaction in alkali and acid electrolytes, *Front. Chem.*, 2019, **7**, 716.
82 Y. Song, U. Sanyal, D. Pangotra, J. D. Holladay, D. M. Camaioni, O. Y. Gutiérrez and J. A. Lercher, Hydrogenation of benzaldehyde *via* electrocatalysis and thermal catalysis on carbon-supported metals, *J. Catal.*, 2018, **359**, 68–75.
83 U. Sanyal, S. F. Yuk, K. Koh, M. S. Lee, K. Stoerzinger, D. Zhang, L. C. Meyer, J. A. Lopez-Ruiz, A. Karkamkar and J. D. Holladay, Hydrogen bonding enhances the electrochemical hydrogenation of benzaldehyde in the aqueous phase, *Angew. Chem., Int. Ed.*, 2021, **133**, 294–300.
84 M. J. Sims, N. V. Rees, E. J. F. Dickinson and R. G. Compton, Effects of thin-layer diffusion in the electrochemical detection of nicotine on basal plane pyrolytic graphite (BPPG) electrodes modified with layers of multi-walled carbon nanotubes (MWCNT-BPPG), *Sens. Actuators, B*, 2010, **144**, 153–158.
85 G. P. Keeley and M. E. G. Lyons, The effects of thin layer diffusion at glassy carbon electrodes modified with porous films of single-walled carbon nanotubes, *Int. J. Electrochem. Sci.*, 2009, **4**, 794–809.
86 M. Chandrasekaran, M. Noel and V. Krishnan, Glassy carbon surface effects on the electroreduction of aromatic carbonyl compounds: part 1. Benzaldehyde, *J. Electroanal. Chem. Interfacial Electrochem.*, 1991, **303**, 185–197.
87 H. Jin, H. Zhang, J. Chen, S. Mao, Z. Jiang and Y. Wang, A general synthetic approach for hexagonal phase tungsten nitride composites and their application in the hydrogen evolution reaction, *J. Mater. Chem. A*, 2018, **6**, 10967–10975.
88 D. T. Fagan, I. F. Hu and T. Kuwana, Vacuum heat-treatment for activation of glassy carbon electrodes, *Anal. Chem.*, 1985, **57**, 2759–2763.
89 M. K. Hoque, J. A. Behan, S. N. Stamatin, F. Zen, T. S. Perova and P. E. Colavita, Capacitive storage at nitrogen doped amorphous carbon electrodes: structural and chemical effects of nitrogen incorporation, *RSC Adv.*, 2019, **9**, 4063–4071.
90 E. Pop, V. Varshney and A. K. Roy, Thermal properties of graphene: fundamentals and applications, *MRS Bull.*, 2012, **37**, 1273–1281.
91 W. Zheng, iR compensation for electrocatalysis studies: considerations and recommendations, *ACS Energy Lett.*, 2023, **8**, 1952–1958.
92 J. M. Yoo, H. Shin, D. Y. Chung and Y.-E. Sung, Carbon shell on active nanocatalyst for stable electrocatalysis, *Acc. Chem. Res.*, 2022, **55**, 1278–1289.
93 E. S. Chan-Shing, D. Boucher and J. Lessard, The electrochemical reduction of α-nitrocumene in a protic and basic medium on large surface area (porous) electrodes: electronation-protonation or electrocatalytic hydrogenation?, *Can. J. Chem.*, 1999, **77**, 687–694.
94 H. Chen, J. Iyer, Y. Liu, S. Krebs, F. Deng, A. Jentys, D. J. Searles, M. A. Haider, R. Khare and J. A. Lercher, Mechanism of electrocatalytic H_2 evolution, carbonyl hydrogenation, and carbon–carbon coupling on Cu, *J. Am. Chem. Soc.*, 2024, **146**, 13949–13961.
95 J. A. Lopez-Ruiz, E. Andrews, S. A. Akhade, M.-S. Lee, K. Koh, U. Sanyal, S. F. Yuk, A. J. Karkamkar, M. A. Derewinski, J. Holladay, V.-A. Glezakou, R. Rousseau, O. Y. Gutiérrez and J. D. Holladay, Understanding the role of metal and molecular structure on the electrocatalytic hydrogenation of oxygenated organic compounds, *ACS Catal.*, 2019, **9**, 9964–9972.

